

See discussions, stats, and author profiles for this publication at: <https://www.researchgate.net/publication/316077933>

# Evaluation of retrieval methods of daytime convective boundary layer height based on Lidar data

Article in *Journal of Geophysical Research Atmospheres* · April 2017

DOI: 10.1002/2016JD025620

CITATIONS

39

READS

470

7 authors, including:



Hong Li

Lanzhou University

6 PUBLICATIONS 100 CITATIONS

SEE PROFILE



Yi Yang

Lanzhou University

57 PUBLICATIONS 701 CITATIONS

SEE PROFILE



Zhongwei Huang

Lanzhou University

99 PUBLICATIONS 2,832 CITATIONS

SEE PROFILE



Guoyin Wang

Lanzhou University

20 PUBLICATIONS 3,336 CITATIONS

SEE PROFILE

## RESEARCH ARTICLE

10.1002/2016JD025620

## Key Points:

- Convective boundary layer heights are retrieved from micropulse lidar data where the background counts vary over orders of magnitude
- Four methods of retrieving the CBLH are evaluated, and parameter sensitivities of the retrieval methods are examined
- Boundary layer heights from micropulse lidar data are compared with the boundary layer heights estimated from L-band radiosonde data

## Correspondence to:

Y. Yang,  
yangyi@lzu.edu.cn

## Citation:

Li, H., Y. Yang, X.-M. Hu, Z. Huang, G. Wang, B. Zhang, and T. Zhang (2017), Evaluation of retrieval methods of daytime convective boundary layer height based on lidar data, *J. Geophys. Res. Atmos.*, 122, 4578–4593, doi:10.1002/2016JD025620.

Received 8 JUL 2016

Accepted 7 APR 2017

Accepted article online 12 APR 2017

Published online 30 APR 2017

## Evaluation of retrieval methods of daytime convective boundary layer height based on lidar data

Hong Li<sup>1</sup>, Yi Yang<sup>1</sup> , Xiao-Ming Hu<sup>2</sup>, Zhongwei Huang<sup>1</sup>, Guoyin Wang<sup>1</sup>, Beidou Zhang<sup>1</sup>, and Tiejun Zhang<sup>1,3</sup> 

<sup>1</sup>Key Laboratory of Arid Climatic Changing and Reducing Disaster of Gansu Province, Key Laboratory for Semi-Arid Climate Change of the Ministry of Education, College of Atmospheric Sciences, Lanzhou University, Lanzhou, China, <sup>2</sup>Center for Analysis and Prediction of Storms, and School of Meteorology, University of Oklahoma, Norman, Oklahoma, USA, <sup>3</sup>Institute of Arid Meteorology, China Meteorological Administration, Lanzhou, China

**Abstract** The atmospheric boundary layer height is a basic parameter in describing the structure of the lower atmosphere. Because of their high temporal resolution, ground-based lidar data are widely used to determine the daytime convective boundary layer height (CBLH), but the currently available retrieval methods have their advantages and drawbacks. In this paper, four methods of retrieving the CBLH (i.e., the gradient method, the idealized backscatter method, and two forms of the wavelet covariance transform method) from lidar normalized relative backscatter are evaluated, using two artificial cases (an idealized profile and a case similar to real profile), to test their stability and accuracy. The results show that the gradient method is suitable for high signal-to-noise ratio conditions. The idealized backscatter method is less sensitive to the first estimate of the CBLH; however, it is computationally expensive. The results obtained from the two forms of the wavelet covariance transform method are influenced by the selection of the initial input value of the wavelet amplitude. Further sensitivity analysis using real profiles under different orders of magnitude of background counts show that when different initial input values are set, the idealized backscatter method always obtains consistent CBLH. For two wavelet methods, the different CBLH are always obtained with the increase in the wavelet amplitude when noise is significant. Finally, the CBLHs as measured by three lidar-based methods are evaluated by as measured from L-band soundings. The boundary layer heights from two instruments coincide with  $\pm 200$  m in most situations.

### 1. Introduction

The atmospheric boundary layer, also known as the planetary boundary layer, is the lowest layer of the atmosphere [Stull, 1988]. It is therefore directly affected by surface conditions and in turn has a major influence on the planetary ecosystem. In this layer, turbulent mixing modulates the variation in temperature, flow velocity, moisture, and atmospheric composition and so acts as a bridge between the free troposphere and surface for the exchange of matter, energy, and moisture [Stull, 1988]. In studies of the boundary layer, the boundary layer height has received considerable attention, especially as an important element in boundary layer parameterization, pollutant diffusion, the study of boundary layer structure, and other issues [Stull, 1988; Hu et al., 2010a].

Over land, the boundary layer displays a diurnal evolution responding to the sensible heat flux at the surface. During the day, solar heating causes the surface to warm and elevated turbulence is generated in the lower 1–2 km above the ground, which is referred to as the mixed layer. This well-mixed layer is often capped by a stable layer, which can entrain the drier air from the free atmosphere into the mixed layer, and thus, the stable layer is known as the entrainment zone. After sunset, turbulence in the mixed layer decays, and the upper portion of the mixed layer becomes the statically neutral residual layer [Hu, 2015].

Various empirical formulae have been used to estimate the boundary layer height from ground-based observations [e.g., Elliott, 1958; Hanna, 1987]. Each formula has its limitations (e.g., strict assumptions) and such estimates of the boundary layer height can be crude. Other more reliable methods have been used to retrieve the boundary layer height. As the convective boundary layer (CBL) is characterized by turbulent fluctuations [André et al., 1978], it can be determined from a proxy of the turbulence [Lange et al., 2015]. For instance, in the entrainment zone, materials are not fully mixed, and the abrupt decrease in turbulence intensity at the top of this layer causes a sharp increase in potential temperature [Gryning and Batchvarova, 1994;

Dang et al., 2016], and this characteristic can be used to designate the CBLH [Huang et al., 2016]. In addition, the boundary layer is more humid than the free atmosphere above, and a strong humidity gradient exists at the top of the boundary layer that can also be used to designate the CBLH [White et al., 1991].

With the ongoing development of modern measurement technologies, approaches for CBLH detection using various measured profiles (e.g., vertical profiles of potential temperature and water vapor mixing ratio) have become increasingly popular. However, although the use of sounding profiles to retrieve the CBLH is straightforward, the temporal resolution of sounding data is normally low [Seibert et al., 2000]. Tower observations provide continuous vertical profiles of meteorological variables but mostly only cover the lower few hundred meters of the boundary layer. A few other profiling methods can provide profiles with higher temporal resolution. Wind profiler radar provides backscatter profiles that are related to moisture within the boundary layer and have a high spatial and temporal resolution, and microwave radiometers provide temperature and humidity observations continuously from the surface up to 10 km. In addition, Aircraft Meteorological Data Reporting provides vertical profiles of some atmospheric elements during commercial aircraft takeoffs and landings [Hu et al., 2010a; Ding et al., 2015; Rahn and Mitchell, 2016]. These multitime data can provide the evolution of boundary layer height over time.

Estimating of the CBLH based on lidar data have received increasing attention over the past decade [Hayden et al., 1997; Flamant et al., 1997; Steyn et al., 1999; Davis et al., 2000; Cohn and Angevine, 2000; Brooks, 2003; Baars et al., 2008; Granados-Muñoz et al., 2012; McGrath-Spangler and Denning, 2012; Lewis et al., 2013; Sawyer and Li, 2013; Pal et al., 2013; Bravo-Aranda et al., 2016]. Lidar returns a profile of backscatter signals from which the CBLH values can be extracted. The main advantage of the lidar approach is that lidar offers real-time monitoring of the atmospheric aerosol loading and structure, which can help diagnose boundary layer structure and its temporal variation.

The determination of the CBLH from lidar is based on the characteristics of the well-mixed CBL. Generally, the aerosol concentration within the boundary layer is much higher than that in the free atmosphere, which results in a decrease in lidar backscatter signal at the boundary layer top. This characteristic can be used to find the CBLH. Due to the incomplete overlap between the laser beam and its receiving optical axis, the lowest few hundred meters are not accurately measured, and the nighttime stable boundary layer may be shallower than the lidar overlap range [Sicard et al., 2006; Di et al., 2013; Sawyer and Li, 2013]. Besides, certain problems also remain, e.g., in the presence of optically thick clouds, which may complicate the CBLH retrieval process because of the high signal gradient generated by clouds [Davis et al., 2000; Hennemuth and Lammert, 2006]. Thus, this study only focuses on the convective boundary layer during daytime under a clear-sky over land.

At present, CBLH retrieval methods based on lidar data include subjective visual estimates [Boers et al., 1984; Nelson et al., 1989], the threshold method [Melfi et al., 1985], the gradient method [Hayden et al., 1997], the inflection point method [Menut et al., 1999], the idealized backscatter method [Steyn et al., 1999], the maximum deviation method [Hooper and Eloranta, 1986; Lammert and Bösenberg, 2006], and the wavelet covariance transform method [Davis et al., 2000; Brooks, 2003; Morille et al., 2007]. These methods each have their own benefits and limitations. Visual estimates are simple but subjective, and visual errors are inevitable [Boers et al., 1984]. This approach also precludes automated determination of the CBLH. For the threshold method, the CBLH is defined as the height where the backscatter intensity first exceeds a given threshold when subsiding downward from the free unpolluted troposphere. Since simple signal threshold values are used, this method is therefore sensitive to the threshold values [Emeis et al., 2008]. The gradient method uses the negative peak of the first derivative of the range-corrected signal [Hayden et al., 1997] or the logarithm of the range-corrected signal [Senff et al., 1996] to detect the CBLH. The inflection point method is also a type of gradient method, which takes the minimum of the second derivative of the range-corrected signal as the indication for the CBLH [Menut et al., 1999]. The gradient and inflection point methods are simple and easy to use, but they are easier to be affected by signal noise and atmospheric variability [Hennemuth and Lammert, 2006]. In practical observations, the structure within the boundary layer is more complex than in the free unpolluted atmosphere, meaning that the fluctuation of the signal is large. Consequently, the applicability of the gradient and inflection point methods is limited [Z. Wang et al., 2012].

The idealized backscatter method is also an extension of the gradient method, in which the CBLH is not determined from the observed lidar backscatter profile, but from an idealized backscatter profile fitted to the

observed profile. A process of multidimensional minimization is needed to determine the best fit values for the profile parameters, and the implementation of the method of simulated annealing achieves satisfactory results but with a relatively little computational cost compared with the downhill simplex method [Steyn *et al.*, 1999].

Within the entrainment zone, vertical turbulence mixes aerosol laden air with cleaner free tropospheric air. Such mixture produces a large variance in the lidar backscatter signal, which can be used as an indicator of the entrainment layer [Hooper and Eloranta, 1986; Lammert and Bösenberg, 2006]. The variance method is therefore susceptible to the noise caused by the lidar itself or interference from the aerosol layer [Z. Wang *et al.*, 2012; Emeis *et al.*, 2008]. The wavelet method, based on the Haar mother function [Davis *et al.*, 2000; Cohn and Angevine, 2000], requires fewer computational resources and has been developed for the automatic determination of CBLH from lidar backscatter signals.

Within this context, this paper evaluates four different lidar-based retrieval methods for CBLH and compares them with the conventional retrieval method based on radiosonde data. Section 2 describes the data set. The methods commonly used to retrieve the CBLH based on lidar and radiosonde data are described in detail in section 3. Four lidar-based retrieval methods are applied to two synthetic profiles to retrieve CBLH in section 4. Besides, real profiles on 2 days with background counts ranging across different orders of magnitude are used to test the CBLH estimated by the idealized backscatter method and two forms of the wavelet methods, and the empirical initial values of each methods are presented in section 4. The estimated CBLHs from lidar-based methods are also compared with the CBLHs estimated from radiosonde data in section 4.4. Section 5 presents conclusions and discussion.

## 2. Data Sets

### 2.1. Micropulse Lidar

Micropulse lidar (MPL) has become an important active remote sensing tool in recent years because of its high accuracy, high spatiotemporal resolution, wide detection range, and eye-safe emitted energy. Spinhirne [1993] described the basic principles of MPL. MPL is widely used in continuous, automatic observations of atmospheric aerosols and clouds. For instance, lidar data can be used to calculate aerosol extinction and optical thickness profiles [Spinhirne, 1993; Welton *et al.*, 2002], detect clouds and aerosol layers [Zhao *et al.*, 2014], and trace the boundary layer [Lammert and Bösenberg, 2006].

The MPL data used in this study are obtained from the Semi-arid Climate Observatory and Laboratory of Lanzhou University (SACOL), which is located at Yuzhong at an elevation of 1961 m (35.946°N, 104.137°E). At SACOL, an MPL-4 records backscatter signals up to 20+ km at intervals of 1 min [Huang *et al.*, 2010]. The lidar data used has a vertical resolution of 75 m in 2007, while 30 m in 2011. The lidar equation can be expressed as [Fernald *et al.*, 1972]

$$P(z) = CE\beta(z)T^2(z)/z^2, \quad (1)$$

where  $P(z)$  is the received signal from a scattering volume at height  $z$ ,  $C$  is the lidar constant,  $E$  is the lidar pulse energy,  $\beta(z)$  is the backscatter coefficient, and  $T(z)$  is the integral of the extinction coefficients from 0 to  $z$ . After range correcting and laser energy normalizing, a variable referred to as normalized relative backscatter  $B0(z)$  (NRB) is derived in equation (1)

$$B0(z) = \frac{P(z)z^2}{E} = C\beta(z)T^2(z) = C\beta(z)\exp(-2T(z)). \quad (2)$$

This value has been overlap corrected and with the background and dark count correction terms removed. Signals between 45 and 55 km are averaged to estimate the sum of background and dark counts [Campbell *et al.*, 2002].

### 2.2. Radiosonde

We also compare the boundary layer heights retrieved from the lidar data with those determined from L-band radiosonde temperature profiles at Yuzhong (35.87°N, 104.15°E, approximately 8.83 km away from SACOL with an elevation of 1875 m above sea level). The L-band radiosonde is launched twice a day, i.e.,

0000 and 1200 UTC (0800 and 2000 local time) at Yuzhong as part of the L-band radiosonde network deployed by the China Meteorological Administration (CMA). The L-band radiosonde network uses the GTS1 digital electronic radiosonde and provides profiles of meteorological variables at fine vertical resolution (recorded every second during the launching process). Previous studies evaluated the accuracy of GTS1 observations [Tao et al., 2006; Bian et al., 2011] and indicated that the GTS1 radiosondes provide temperature profiles as accurate as the Vaisala RS80 profiles in the troposphere. The fine-resolution L-band radiosonde data have been used to study boundary layer features across China [Zhang et al., 2008; Yang et al., 2011; Zhang et al., 2011; Du et al., 2013; Guo et al., 2016].

### 3. Introduction to CBLH Detection Methods Based on Lidar and Radiosonde Data

#### 3.1. Retrieval of Boundary Layer Heights From Lidar Backscatter Data

The retrieval of the CBLH using lidar data is based on the distribution of aerosol particles. Since the passive constituents (e.g., aerosols and gases) are highly mixed in the CBL and therefore large gradients of aerosol concentration occur at the top of the CBL, the CBLH can be estimated from the steepest gradient in the lidar backscatter signal.

##### 3.1.1. Idealized Backscatter Method

The idealized backscatter method [Steyn et al., 1999], which is also known as curve fitting (hereafter *fitting*), is based on fitting a four-parameter ideal profile. In this method, an ideal backscatter profile  $B(z)$  is fitted to the observed backscatter profile  $B0(z)$  by minimizing the measure of agreement between the two profiles. The ideal backscatter profile,  $B(z)$ , can be expressed as

$$B(z) = \frac{(B_m + B_u)}{2} - \frac{(B_m - B_u)}{2} \operatorname{erf}\left(\frac{z - z_m}{s}\right), \quad (3)$$

where  $\operatorname{erf}(a)$  is the error function, expressed as

$$\operatorname{erf}(a) = \frac{2}{\sqrt{\pi}} \int_0^a \exp(-y^2) dy, \quad (4)$$

where  $B_m$  and  $B_u$  are the average values of the backscatter signal within the mixed layer and above the entrainment layer, respectively. The parameter  $z_m$  is the top height of the CBL (the middle of the entrainment layer), and the parameter  $s$  is related to the thickness of the entrainment zone. The entrainment zone thickness (EZT) in this case has a depth which is equal to 2.77 times the value of  $s$  [Steyn et al., 1999]. Eresmaa et al. [2006] assuming that  $A1 = \frac{(B_m + B_u)}{2}$  is a constant during the calculation and pointed out that the selection of  $A1$  could directly affect the quality of the results. The parameter  $A1$  is determined both based on the atmospheric stability and the structural features of the lidar signal profile, so that the initial order of magnitude of  $A1$  is difficult to identify. However, the initial orders of magnitude of  $z_m$  and  $s$  are relatively easy to determine and are assumed to be constants in our calculations.

Once  $z_m$  and  $s$  have been determined, the mixed layer height and entrainment layer height can be calculated from  $z_m - 0.5 \text{ EZT}$  and  $z_m + 0.5 \text{ EZT}$ , respectively. Thus, in practice, the initial estimates of  $z_m$  and  $s$  are given in the calculation process first. Then, along with the increasing iterations, many groups of  $z_m$ ,  $s$  can be obtained through a process of multidimensional minimization, and we are more likely get the true estimate of CBLH (i.e., the value of  $z_m$  that minimizes  $\sum (B(z) - B0(z))^2$  is assumed to be the actual CBLH).

Steyn et al. [1999] are the first to use the downhill simplex method to achieve the multidimensional minimization, but they then showed that the method is not reliable and applied the simulated annealing algorithm. This new algorithm is able to generate satisfactory results from fewer calculations. However, Sawyer and Li [2013] pointed out that the simulated annealing algorithm was only applied to airborne lidar data by Steyn et al. [1999]. Airborne lidar is a limited temporal instrument, and the initial values are relatively easy to provide. For ground-based lidar, continuous retrieval of the CBLH can be achieved, and therefore, it is difficult to provide a proper initial value because the CBLH changes significantly through the day. The retrieval results of the curve-fitting method based on the simulated annealing algorithm obviously depend on the selection of the initial value. In this paper, although we do use the simulated annealing algorithm to obtain the CBLH as

precisely as possible, the searching range and times of  $z_m$  and  $s$  during the searching process are extended, and a limitation of  $z_m - 0.5 \text{ EZT} > 0$  is utilized in the searching process.

### 3.1.2. Gradient Method

The gradient method (GM) is proposed by *Hayden et al.* [1997]. It defines the altitude corresponding to the maximum decay velocity at the vertical of the signal as the CBLH and is expressed as

$$g(z) = -\frac{d[B(z)]}{dz}, \tag{5}$$

where  $dz$  is the vertical resolution of the lidar data and  $g(z)$  is the first derivative of the optical backscatter intensity  $B(z)$ . The largest value of  $g(z)$  is associated with the greatest decay velocity of the signal. Thus, the height that corresponds to the largest peak of  $g(z)$  is regarded as the CBLH.

### 3.1.3. Wavelet Method

The wavelet method is developed for automatic determination of the CBLH. The most significant advantage of this method is that the time and frequency characteristics of the signal are highlighted by means of wavelet analysis [*Farge, 1992*].

The method is based on a wavelet covariance transform,  $W_f(\Delta h, z_m)$ , which is defined as

$$W_f(\Delta h, z_m) = \frac{1}{\Delta h} \int_{z_b}^{z_t} f(z) \varphi\left(\frac{z - z_m}{\Delta h}\right) dz, \tag{6}$$

where  $f(z)$  is an objective function of integral;  $\varphi\left(\frac{z - z_m}{\Delta h}\right)$  is the mother function of the wavelet method; the parameters  $z_b$  and  $z_t$  are the floor and ceiling of the integral, respectively;  $\Delta h$  indicates the amplitude of the mother function; and  $z_m$  indicates the center position of the mother function as well as the location of the CBLH.

There are several mother functions available, and the choice of function has a specific influence on the results. In this paper, the Haar and Mexican Hat wavelet mother functions are chosen as they have been frequently used as mother functions in previous studies [*Davis et al., 2000; Lopes et al., 2014*].

As significant reduction in the lidar backscatter signal occurs at the layer between the mixed layer and the free atmosphere, the step change in signal is similar to the step characteristic of the Haar wavelet. Consequently, we use the Haar wavelet mother function along with the backscatter profile,  $B0(z)$ , as  $f(z)$  to estimate the CBLH (i.e., the Haar method, hereafter referred to as the HM). The Haar wavelet is expressed as

$$\varphi\left(\frac{z - z_m}{\Delta h}\right) = \begin{cases} 1, & z_m - \frac{\Delta h}{2} \leq z \leq z_m \\ -1, & z_m \leq z \leq z_m + \frac{\Delta h}{2} \\ 0, & \text{else} \end{cases} \tag{7}$$

As the Haar wavelet analysis is applied to  $B0(z)$ , equation (6) allows for a comparison between the backscatter profile and the Haar wavelet function across a vertical range from  $z_m - \Delta h/2$  to  $z_m + \Delta h/2$ . The parameter  $W_f$  represents the similarity between them, i.e., the larger value of  $W_f$ , the greater the similarity. Thus, the height of  $z_m$  where  $W_f$  reaches its maximum should be regarded as the CBLH. The parameter  $\Delta h$  is the dilation of the Haar wavelet and corresponds to the thickness of the entrainment zone physically, and equals  $2dz, 4dz, 6dz, \dots$

The significant signal loss at the height of the CBL corresponds to the maximum of the signal gradient profile  $g(z)$ , the shape of which is the same as the Mexican Hat wavelet. Consequently, the Mexican Hat wavelet mother function can be applied to  $g(z)$ , which is  $f(z)$  in equation (6), to identify the CBLH (i.e., the Mexican Hat method, hereafter referred to as the MHM). The Mexican Hat function is defined as [*Zhou and Adeli, 2003*]

$$\varphi\left(\frac{z - z_m}{\Delta h}\right) = \left[1 - \left(\frac{z - z_m}{\Delta h}\right)^2\right] \exp\left[-\frac{1}{2} \left(\frac{z - z_m}{\Delta h}\right)^2\right]. \tag{8}$$

The difference from the Haar function is that when the value of  $g(z)$  is maximized,  $W_f$  is also maximized, and the corresponding  $z_m$  is taken to be the CBLH. Here  $\Delta h$  also indicates the thickness of the entrainment zone.

### 3.2. Retrieval of Boundary Layer Heights From the L-Band Radiosonde Data

Various methods have been proposed to estimate the boundary layer height from vertical profiles of temperature, potential temperature, or other variables [Hennemuth and Lammert, 2006; Nielsen-Gammon et al., 2008; Seidel et al., 2010; Guo et al., 2016]. In this study, the 1.5-theta-increase method [Nielsen-Gammon et al., 2008] is chosen to estimate the CBLH from the L-band radiosonde data because the method is less sensitive to soundings' vertical resolution than other methods based on a vertical derivative. The 1.5-theta-increase method defines the CBLH as the height where the potential temperature first exceeds the minimum potential temperature within the boundary layer by more than 1.5 k. This method has been applied to estimate continental CBLH [e.g., Hu et al., 2010a] and marine boundary layer heights [e.g., Hu et al., 2010b].

## 4. Analysis of Stability and Case Study

### 4.1. Artificial Profile Experiment

In this section, the lidar-based methods outlined above are compared by using two synthetic profiles: an idealized profile and a simulated real profile. The idealized profile ( $B_0$  in Figure 1a) of  $z_m = 1500$  m and  $s = 100$  m is constructed referring to equation (3). According to  $EZT = 2.77$  s, the thickness of the entrainment zone is 277 m (the vertical resolution of the profile is 15 m). The top of the mixed layer, that is  $z_m - 0.5$  EZT, is 1361.5 m. By the same token, the top of the entrainment zone ( $z_m + 0.5$  EZT) is 1638.5 m. Then, to simulate the actual lidar backscatter profile, a simulated real profile ( $B_0$  in Figure 1c) is constructed by adding Gaussian perturbations to  $B_0$  in Figure 1a referencing the error spectra of lidar presented by Tao et al. [2009].

First, the fitted profile of the idealized profile is shown as  $B$  in Figure 1a, and the CBLH derived by *fitting* (the initial value of  $z_m$  is set to 600 m) is 1499 m (solid purple line in Figure 1a). The retrieval result indicates that this method has no difficulty in detecting the CBLH in the ideal situation. For the simulated real profile, the fitted profile is shown as  $B$  in Figure 1c, and the CBLH derived by *fitting* is 1500 m (the solid purple line in Figure 1c), which is also reliable.

To test the result of GM, the gradient profile of the idealized profile and the simulated real profile are calculated and are shown as  $g$  in Figures 1b and 1d, respectively (blue dashed lines). The CBLH estimated from the idealized profile by GM is 1433 m, which is close to the mixed layer top. However, for the simulated real profile, the perturbations of the signal in the lower layers have a large impact on the distribution of the gradient values and the CBLH estimated by GM is 818 m, which is obviously incorrect. Consequently, GM is only suitable for nearly ideal conditions. Therefore, GM is not recommended to use alone.

The Haar wavelet coefficient profile  $W_f$  for the idealized profile is shown as the black dashed line in Figure 1b, and the CBLH retrieved by HM is 1500 m, corresponds to the height of the maximum of  $W_f$ , which is also the center height of the entrainment zone (black solid line in Figure 1b). The calculated Haar wavelet coefficient profile  $W_f$  for the simulated real profile is shown as the black dashed line in Figure 1d, and it is easy to see that even if small signal perturbations exist, the maximum value of  $W_f$  occurs at a height of 1500 m, which is the intended CBLH (black solid line in Figure 1d).

Similarly, the Mexican Hat wavelet coefficient profile  $W_f$  for the idealized profile is shown as the red dashed line in Figure 1b. The CBLH retrieved by MHM is 1500 m, the center height of the entrainment zone (red solid line in Figure 1b). For the simulated real profile, the Mexican Hat wavelet coefficient profile  $W_f$  is shown as the red dashed line in Figure 1d, from which we can see that even if many local maxima of  $W_f$  are present, the maximum value of  $W_f$  still occurs at a height of 1500 m (red solid line in Figure 1d).

Therefore, for either idealized or simulated real profile, *fitting*, HM, and MHM can all generate reliable results. However, for the GM used in this paper, we see that under conditions in which the noise is obvious, the result is not reliable and GM is not recommended to use alone.

### 4.2. Stability Analysis

An initial value of  $z_m$  must be given when *fitting* is applied. Likewise, initial values of  $\Delta h$  are needed for HM and MHM. Different values of  $z_m$  or  $\Delta h$  may generate different CBLH. Consequently, *fitting*, HM, and MHM

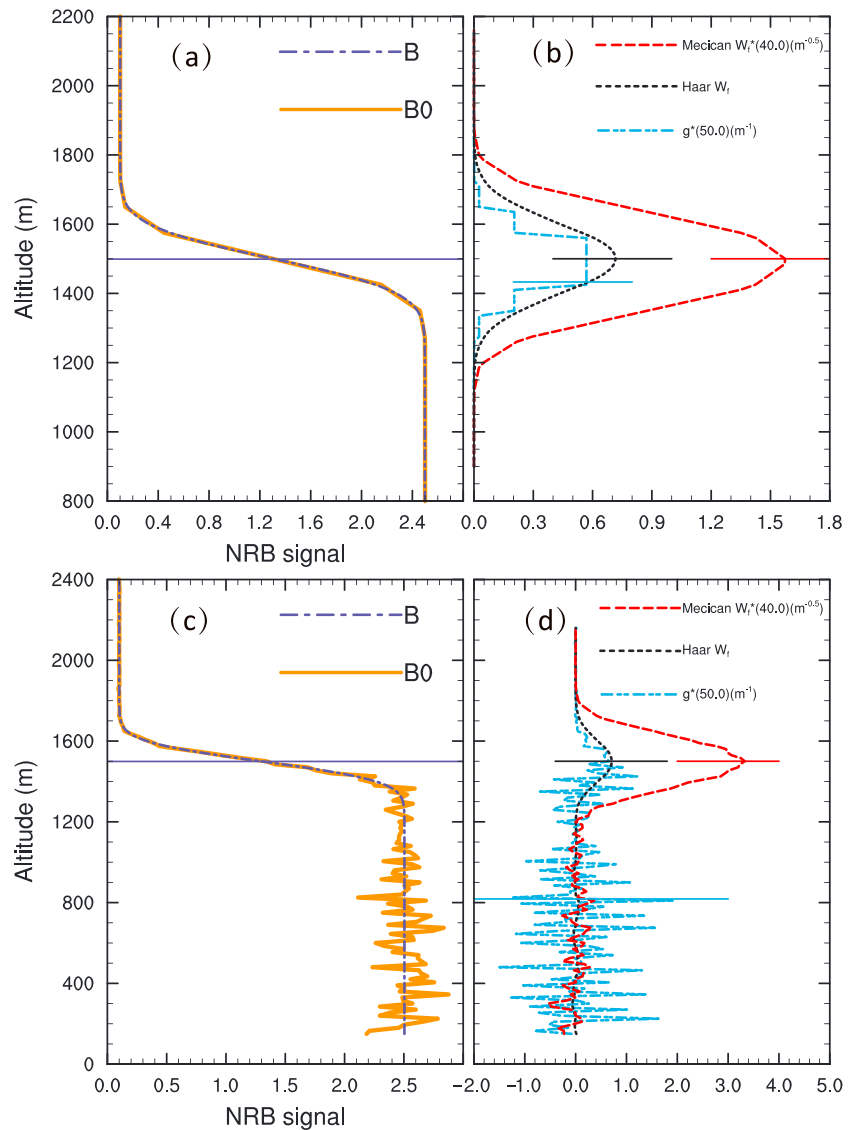


**Figure 1.** (a) The idealized profile and (c) the simulated real profile of the normalized relative backscatter signal (NRB) ( $B_0$ ) along with the fitted curve  $B$ , and (b and d) the corresponding profiles of gradient  $g$ , the Haar wavelet coefficient (Haar  $W_p$ ), and the Mexican Hat wavelet coefficient (Mexican  $W_p$ ). The CBL tops identified from those profiles are marked by the horizontal lines.

are used on the synthetic idealized and simulated real profiles; simultaneously, different values of  $z_m$  or  $\Delta h$  are applied to the corresponding method to test their stability. The results are shown in Figures 2a and 2b, and it is evident that *fitting* is the most stable method compared with the other two wavelet methods. For the synthetic idealized profile, with an increase in the value of  $\Delta h$ , the result of HM becomes stable. But for MHM, there is always a slight variation around the real CBLH value as  $\Delta h$  increases. However, for the simulated real profile, HM immediately becomes stable with the increase in  $\Delta h$ , but the variation of MHM becomes larger with the increase in  $\Delta h$  (Figure 2b).

**4.3. Real Profiles in Well-Mixed Convective Boundary Layers**

Figure 3 shows two clear-sky cases (i.e., 19 December and 16 July 2007) measured at SACOL. On each day, the CBLH are calculated by *fitting*, HM, and MHM at time intervals of 10 min (the NRB are averaged every 11 min) from 08:05 to 19:55 local time. As can be seen from the Figure 3, the CBL heights from *fitting* show good time continuity and agree well with typical diurnal variation of CBLH on 19 December and 16 July 2007.

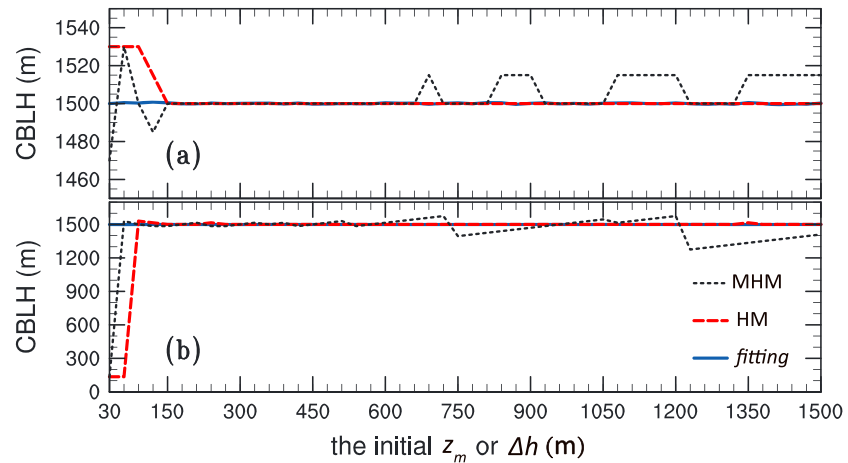


**Figure 2.** The CBLH calculated by using the idealized backscatter method (*fitting*), Haar wavelet method (HM), and Mexican Hat method (MHM) with different initial values of  $z_m$  or  $\Delta h$  set for (a) the idealized profile and (b) the simulated real profile.

Meanwhile, the CBL heights from HM and MHM are always similar. However, sudden changes in the retrieved CBLH by wavelet methods are more likely to occur (see Figure 3a). This also confirms our previous results that *fitting* is more robust than wavelet methods.

The method *fitting* not only defines the CBLH robustly but also provides the information of EZT. In previous studies, the measurements of EZT are rare and hard to validate. In theory, the entrainment zone is usually defined to be the region in which the mean buoyancy flux is negative [Driedonks and Tennekes, 1984]. From the method *fitting*, the EZT is the region where aerosol profile has strong gradients. We examine and present the evolution of the EZT on selected days. It is easy to see that on the winter case selected (19 December 2007; Figure 4), the lidar backscatter signal decreases at low height, which means that the EZT can be even lower than our lidar valid detection range. So here, we only discuss the summer case (i.e., 16 July 2007). The daily evolution of EZT from lidar data is shown as the portion between the red solid line

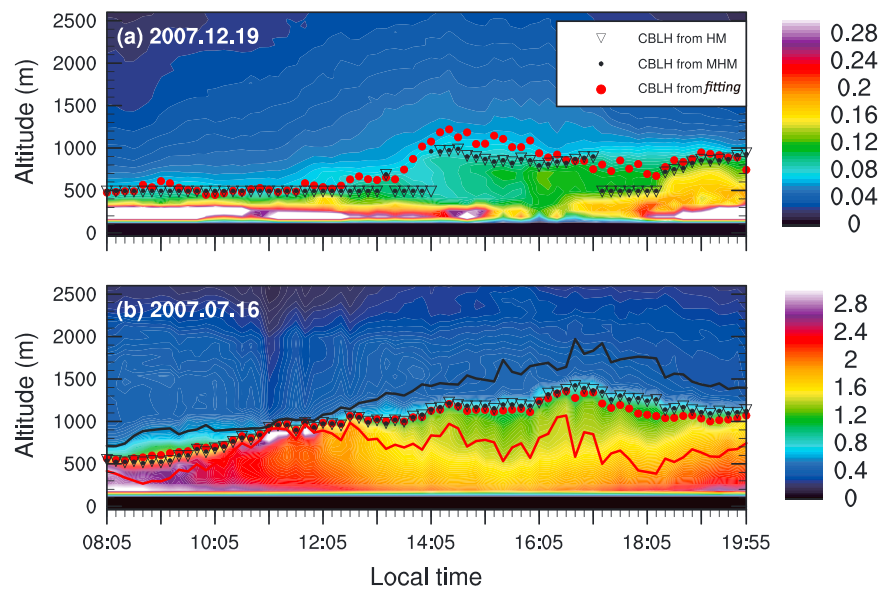


**Figure 3.** Time-height diagram of the NRB (averaged every 11 min) on (a) 19 December and (b) 16 July 2007. The CBL tops during 08:05 to 19:55 local time at time intervals of 10 min diagnosed by using the idealized backscatter method (CBLH from *fitting*), Mexican Hat wavelet method (CBLH from MHM), and Haar wavelet method (CBLH from HM) are marked. The initial value of  $z_m$  (used by *fitting*) or  $\Delta h$  (used by HM and MHM) is set to 300 m. The red line and black line in Figure 3b represent the bottom and the top of the entrainment zone, respectively.

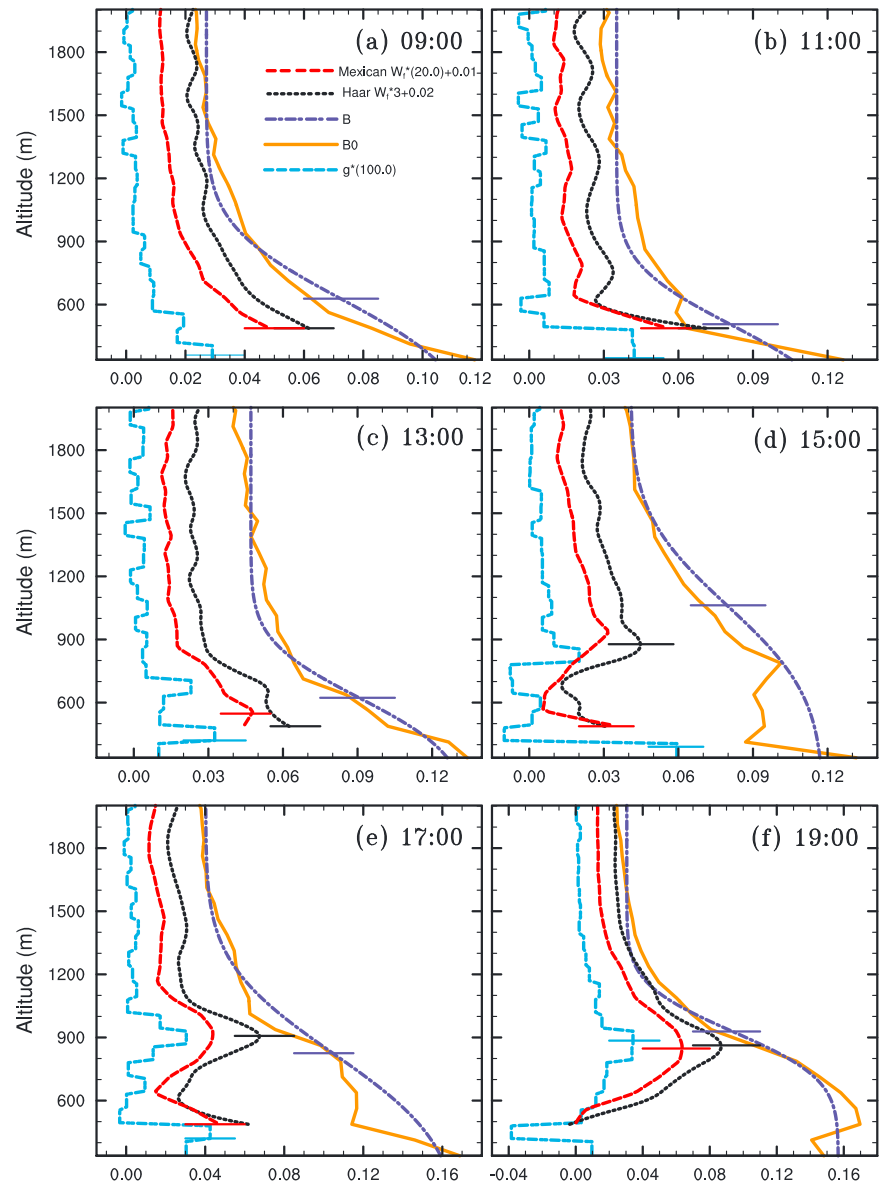


**Figure 4.** The real profile of the normalized relative backscatter signal ( $B_0$ ) with the corresponding profiles of gradient ( $g$ ), Haar wavelet coefficient (Haar  $W_{\beta}$ ), Mexican Hat wavelet coefficient (Mexican  $W_{\beta}$ ), and fitted profile ( $B$ ) at (a) 09:00, (b) 11:00, (c) 13:00, (d) 15:00, (e) 17:00, and (f) 19:00 local time on 19 December 2007. The CBL tops identified from those profiles are marked by the horizontal lines.

and the black solid line in Figure 3b. It is clear that after sunrise, as the mixing layer deepens, the depth of “entrainment zone” (the residual layer from the day before) decreases until about 11:25 local time. Then the period from 11:25 to 14:00 local time is marked by an enlarged EZT; this may be caused by the increased radiation flux. However, after 14:00 local time, the depth of EZT changes little over time.

To further test the actual performance of the three methods and how sensitive they are to the initial values, we use NRB profiles at six different times (09:00, 11:00, 13:00, 15:00, 17:00, and 19:00 (local time)) on two selected cases ( $B_0$  in Figures 4 and 5). These profiles are from nearly well-mixed continental convective boundary layers, but the background counts are quite different. Background counts always have effect on signals closer to the surface, nearly few kilometers above the surface. The calculated background counts at different times on two chosen days are estimated by averaging signals from 45 km to 55 km in vertical and are showed as Table 1.

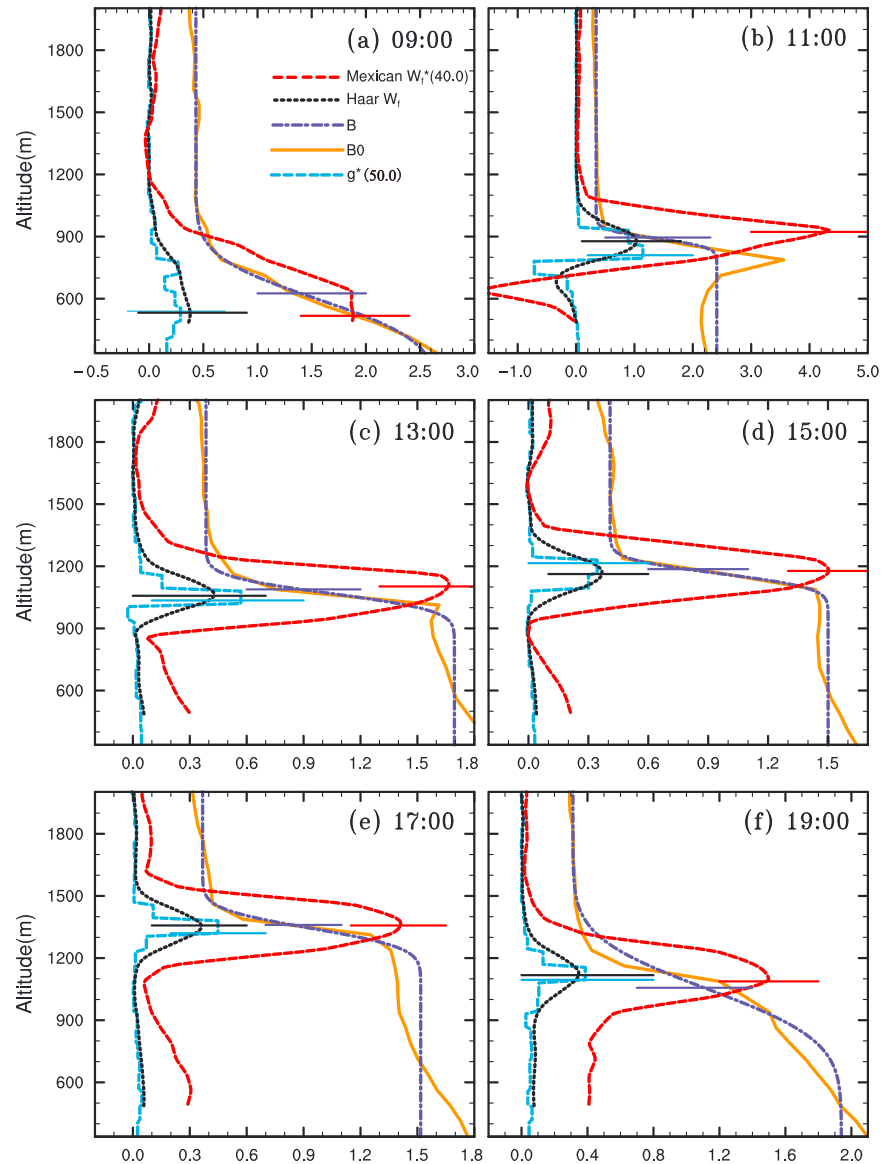


**Figure 5.** The real profile of the normalized relative backscatter signal ( $B_0$ ) with the corresponding profiles of gradient ( $g$ ), Haar wavelet coefficient (Haar  $W_\beta$ ), Mexican Hat wavelet coefficient (Mexican  $W_\beta$ ), and fitted profile ( $B$ ) at (a) 09:00, (b) 11:00, (c) 13:00, (d) 15:00, (e) 17:00, and (f) 19:00 local time on 16 July 2007. The CBL tops identified from those profiles are marked by the horizontal lines.

To generate more precise empirical initial values for the two wavelet methods, the lidar NRB profile data, which have a vertical resolution of 75 m or 30 m, are interpolated to a resolution of 15 m by using a linear interpolation. According to the conclusion of the former analysis, the resulting CBLH generated by *fitting*

always shows a plateau at the correct CBLH. So in this section, the results from *fitting* are regarded as reference values of true CBLH and are used to examine the behavior of the other methods.

Figure 4 shows the CBLH calculated from GM, *fitting*, HM, and MHM by using the real profiles from 19

**Table 1.** Background Counts at Different Times on Two Selected Days

Local Time	19/12/2007	16/7/2007
09:00	5.2074999E - 02	0.1637330
11:00	0.1211850	0.5655600
13:00	0.1462150	1.248242
15:00	0.1192670	0.4928560
17:00	4.0286001E - 02	0.1937110
19:00	1.5900000E - 04	8.1184998E - 02

**Table 2.** CBLH (m) Calculated by Using the Four Different Methods at Six Different Times on Two Different Days

Date	Local Time	CBLH (m) Calculated Using			
		Fitting	HM	MHM	GM
19 December 2007	09:00	628.1	487.5	487.5	360.0
	11:00	506.7	487.5	487.5	345.0
	13:00	622.8	487.5	547.5	420.0
	15:00	1062.4	877.5	487.5	390.0
	17:00	825.2	907.5	487.5	420.0
	19:00	928.5	862.5	847.5	885.0
16 July 2007	09:00	625.6	532.5	517.5	735.0
	11:00	895.4	877.5	922.5	810.0
	13:00	1088.4	1057.5	1102.5	1035.0
	15:00	1186.1	1162.5	1177.5	1215.0
	17:00	1360.0	1357.5	1357.5	1320.0
	19:00	1056.7	1117.5	1087.5	1095.0

December 2007 (the initial value of  $z_m$  or  $\Delta h$  is set to 300 m); correspondingly, the Table 1 shows the minor background counts on the day. Similarly, the result for another day is shown in Figure 5 (16 July 2007). From Figures 4 and 5, the background counts do not matter the smoothness of NRB profiles significantly and cannot describe the noise of profile completely. Obviously, for profiles at different times on different days, the *fitting* method always generates accurate CBLH from these profiles, the CBLH values appear as middle heights of

the entrainment zone (purple solid lines in Figures 4 and 5). However, the calculated CBLH values from GM (blue solid lines in Figures 4 and 5) rise and fall slightly around the middle of the entrainment zone, as do the results from HM and MHM. But sometimes, GM fails to extract actual CBLH because of the interference of the lower layer. The resulting CBLH values on 2 days are listed in Table 2.

Next, we test the stability of *fitting*, HM, and MHM by setting different initial values of  $z_m$  or  $\Delta h$  for the real profiles on 2 days (Figures 6 and 7). The results show that different initial values of  $z_m$  have no effect on the resulting CBLH generated by *fitting* when real profile has only single similar shape as the idealized curve. Also, although small noises exist in profiles, it does not affect the extract of CBLH.

From Figures 6 and 7, it is clear that orders of magnitude of background counts less affect HM and MHM to retrieve CBLH, but the smoothness of real profile really makes sense. If the profile is smooth enough (like  $B_0$  in Figures 5b–5f), then the maximum of gradient is apparent, the profile is highly idealized, and HM always generate consistent CBLH when different initial values of  $\Delta h$  are used. For real profiles at other times, the CBLH derived from HM tend to change slightly when a smaller initial value of  $\Delta h$  is used, but as the value of  $\Delta h$  increases to a certain value, the result begins to grow. The behavior of MHM is not as good as that of HM. Even though for highly idealized profiles (like  $B_0$  in Figures 5b–5f), the obtained CBLH always vary significantly compared to the result from *fitting* and HM. However, for real profiles at other times, when  $\Delta h$  is small,

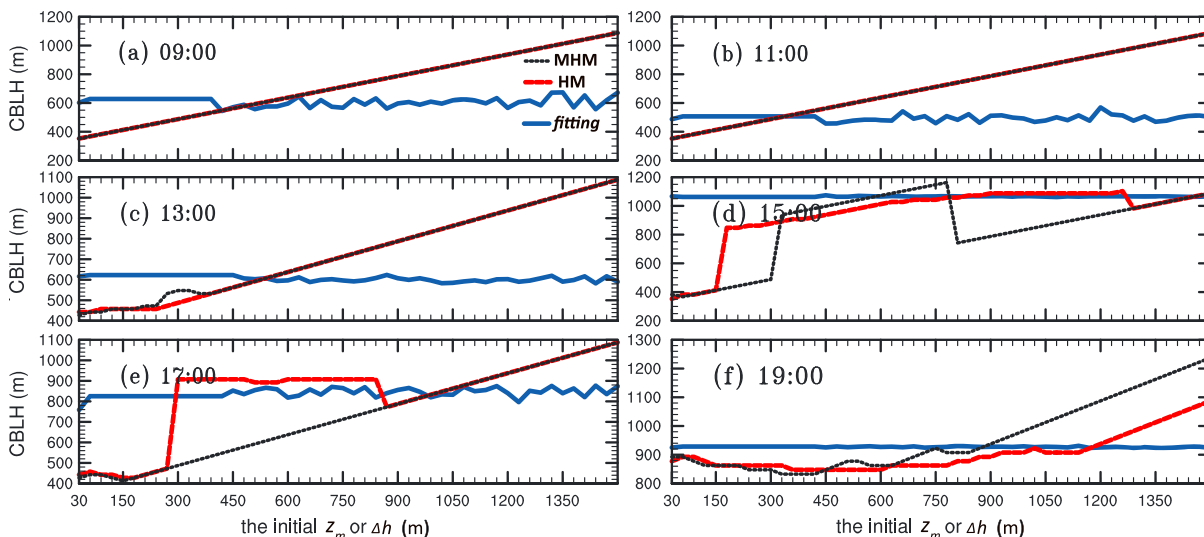


**Figure 6.** The CBL tops identified from the idealized backscatter method (*fitting*), Haar wavelet method (HM), and Mexican Hat wavelet method (MHM) with different initial values of  $z_m$  or  $\Delta h$  being set for the real profiles at (a) 09:00, (b) 11:00, (c) 13:00, (d) 15:00, (e) 17:00, and (f) 19:00 local time on 19 December 2007.

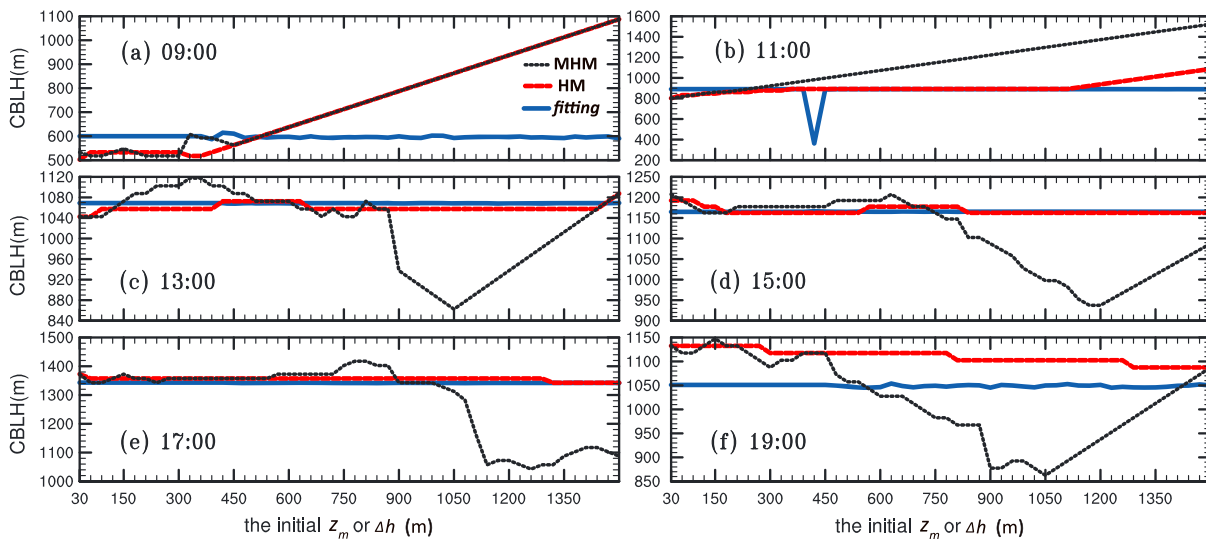


**Figure 7.** The CBL tops identified from the idealized backscatter method (*fitting*), Haar wavelet method (HM), and Mexican Hat method (MHM) with different initial values of  $z_m$  or  $\Delta h$  being set for the real profiles at (a) 09:00, (b) 11:00, (c) 13:00, (d) 15:00, (e) 17:00, and (f) 19:00 local time on 16 July 2007.

the results from MHM are always similar to the CBLH from HM, but when the initial value is large enough, the result from MHM becomes unreliable.

Based on these real cases, the range of  $\Delta h$  values in which the results from HM and MHM plateau at the correct CBLH is different at different times of the same day. However, a constant value of  $\Delta h$  can be used as long as it falls within the plateau range for most real profiles. In this study, for HM and MHM,  $\Delta h$  is held constant at 300 m.

The results obtained from the experiments based on artificial and real data indicate that GM is affected more by signal noise. However, if appropriate initial values are assigned to *fitting*, HM, and MHM, the algorithms will plateau at the correct CBLH. Also, the results show that the initial value of  $z_m$  has no effect on the resulting CBLH generated by *fitting* for profiles which have only single shape similar to the idealized curve, but this is not the case for HM and MHM. Except for highly idealized real profiles, HM can obtain consistent CBLH with different values of  $\Delta h$ , if not, the resulting CBL heights from these two methods vary with the increase of initial values of  $\Delta h$ . And with small values of  $\Delta h$ , HM and MHM are more likely to generate similar value of CBLH. Finally, by studying real profiles at different times on 2 days with different magnitude of background counts, we are able to estimate the empirical value of  $\Delta h$  for most profiles for our site: a  $\Delta h$  value of 300 m for HM and MHM.

#### 4.4. Boundary Layer Heights From Lidar and L-Band Radiosonde

To evaluate the CBLH retrieved from three lidar methods, i.e., *fitting*, HM, and MHM, a comparison of the CBLH determined from lidar and L-band radiosonde data is presented in this section. Radiosondes are launched at 0000 and 1200 UTC (0800 and 2000 local time) at Yuzhong. At 0000 UTC (0800 local time), boundary layer is in stable conditions with a boundary layer height being a few hundred meters derived from radiosonde data. The lidar NRB signals in the lowest few hundred meters are unbelievable for the existence of lidar blind zone caused by incomplete overlap [Sicard *et al.*, 2006; Di *et al.*, 2013; Sawyer and Li, 2013]; thus, lidar data cannot be used to diagnose boundary layer height at 0000 UTC. The soundings at 0000 UTC are therefore left out, and soundings at 1200 UTC are used only. Because the soundings at 1200 UTC (2000 local time) are launched at 1115 UTC (1915 local time) and reached at boundary layer top within 10 min, thus, the lidar NRB signals from 1115 to 1125 UTC are averaged to have a fair comparison. Figure 8a shows the sounding at 1200 UTC on 19 April 2011, and the CBLH estimated by 1.5-theta-increase method is 1012.1 m. At this height, a sharp increase of potential temperature occurs with a concurrent decrease in specific humidity. Figure 8b is the simultaneous lidar NRB signal profile, and the CBLH estimated by *fitting*, HM, and MHM are 870.1 m, 780.0 m, and 787.5 m, respectively.

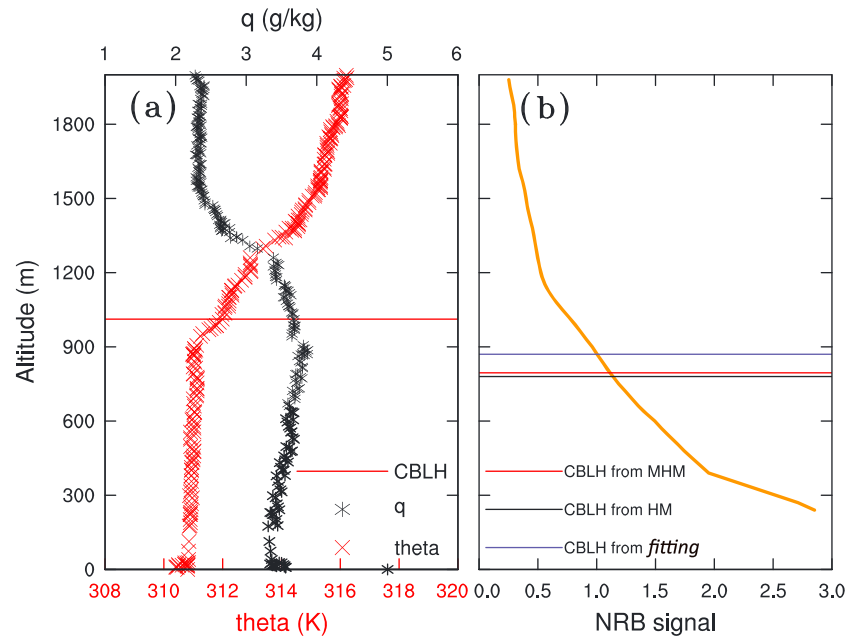


**Figure 8.** Vertical profiles of (a) potential temperature ( $\theta$ ), and specific humidity ( $q$ ) at Yuzhong and (b) NRB at SACOL. The CBLH diagnosed from the profiles by using different methods are marked in each panel. The sounding in Figure 8a is observed at the 1200 UTC on 19 April 2011, and 1.5- $\theta$ -increase method is used to estimate the CBLH. The lidar NRB profile (excludes the signals in the lowest few hundred meters for the existence of lidar blind zone) in Figure 8b is obtained by averaging NRB from 1115 to 1125 UTC on 19 April 2011 at SACOL, and *fitting*, HM, and MHM are used to estimate the CBLH.

From March 2011 to August 2011, because of missing data and cloudy cases rejected, only 18 radiosoundings at 1200 UTC are finally chosen to have a comparison with the results from lidar data. The results are shown in Figure 9. For each of the lidar analysis methods, a good agreement is found with correlation coefficients larger than 0.947. The average bias of the calculated CBLH from the 1.5- $\theta$ -increase method and *fitting*, HM, and MHM are 241.1748 m, 230.4671 m, and 233.8004 m, respectively.

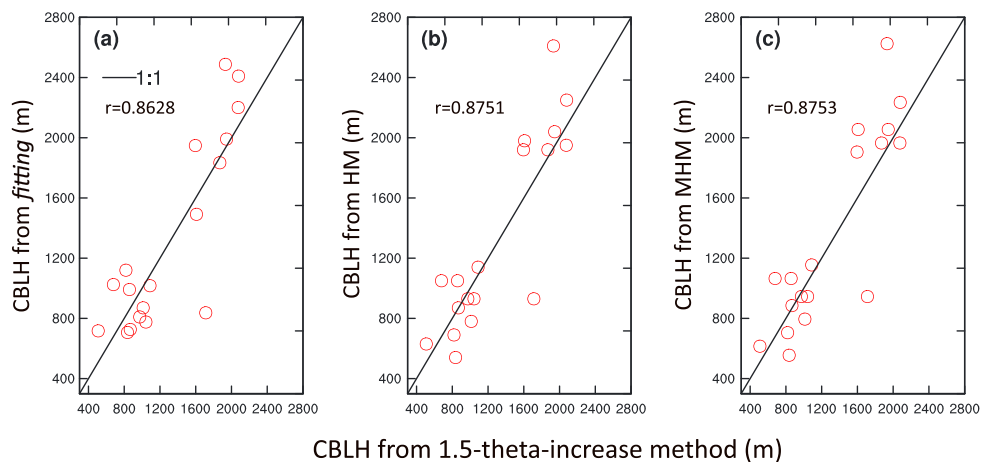


**Figure 9.** Comparison of the CBLH retrieved from the radiosonde data by using 1.5- $\theta$ -increase method with the CBLH retrieved from (a) *fitting*, (b) HM, and (c) MHM. The correlation coefficients (represented by  $r$ ) of the estimated CBLH from 1.5- $\theta$ -increase method and from three lidar methods are showed in the figures.

## 5. Conclusions and Discussion

Ground-based lidar data are widely used to diagnose convective boundary layer height (CBLH) by using various methods. However, the performances of those methods are not well documented under the conditions with different orders of magnitude of background counts of backscatter, which represent the signal noise in some degree. In this article, four methods, i.e., the gradient method (GM), curve fitting (*fitting*), Haar wavelet method (HM), and Mexican Hat wavelet Method (MHM), are used to retrieve the CBLH from lidar backscattering data recorded at Lanzhou, China. Analysis of two synthetic profiles (i.e., an idealized profile and a simulated real profile) and real lidar profiles (from 2 days with different orders of magnitude of background counts) show that the behavior of four methods is different. GM is affected more by signal noise and atmospheric variability. But quite remarkably, the orders of magnitude of background counts cannot represent the noise of signal enough since NRB profiles in high orders of magnitude of background counts are possible to have less noise in signals. Whereas *fitting*, HM, and MHM are able to retrieve the CBLH correctly in most cases with a suitable initial input value being used, especially for *fitting*, which utilizes the entire backscatter profile to make the result more robust. Meanwhile, the obtained CBLH values from HM and MHM show a good agreement in most cases. Results of the CBLH from these three lidar are also compared with the results from L-band radiosonde. The CBL heights estimated from *fitting*, HM, and MHM agree well, and the difference between lidar methods and the 1.5-theta-increase method based on radiosonde data is within  $\pm 200$  m.

In addition, for both synthetic profiles and real profiles, a range from 0 to 1500 m with an interval of 30 m of boundary layer height  $z_m$  (the initial guess for *fitting*) and the wavelet amplitude  $\Delta h$  (the initial guess of the thickness of the entrainment zone for HM and MHM) values are set to evaluate the CBLH retrieval methods. The results indicate that the initial value of  $z_m$  has no effect on the resulting CBLH when *fitting* is applied for profiles with only single shape similar to the idealized curve. This may be due to the method basically fits an idealized curve to the whole real profile, which allows to tolerate more noise and interference in signals.

However, this is not the case for HM and MHM. With different initial values of  $\Delta h$  being set, except for highly idealized profiles (including synthetic profiles and few real profiles) from which HM can obtain consistent CBLH, otherwise, the resulting CBLH from two methods changes a lot. With small values of  $\Delta h$ , HM and MHM are more likely to generate similar CBLH, which is always lower than the result from *fitting*. Large values of  $\Delta h$  are also unsuitable for HM and MHM in most cases. With small values of  $\Delta h$ , problem may arise because the wavelet method is fundamentally a type of gradient method, and the localized features of signal are amplified, which causes spurious gradients and means that error diagnosis would be necessary. However, with the increase in  $\Delta h$ , the signal details are weakened, and the resulting CBLH becomes reliable. But what should be pointed out is that the HM performs better than MHM. Finally, from a study of real profiles, we are able to estimate the empirical values of  $\Delta h$  for most profiles for our site and found that  $\Delta h$  value of 300 m is suitable for HM and MHM. As the selection of the initial parameter will affect the results of these methods, and the empirical value of  $\Delta h$  may vary with the region under study, the value of  $\Delta h$  should be determined through testing.

From this paper, we find that *fitting* method does best in retrieving CBLH automatically. But it is worth noting that the method requires large amount of calculations; i.e., larger search scope and the greater number of searches are needed to find the “best fit” optimal parameter. Yet CBLH from HM is more likely influenced by noise and the input initial value, but with less calculation. Future work will combine these two methods like Sawyer and Li [2013] to extract CBLH effectively.

The presence of clouds may complicate the CBLH retrieval process due to the considerable interference in signals caused by clouds. Attempts have been discussed in recent literatures to deal with cloudy cases, e.g., combine the wavelet technique and image processing to decrease the influence by clouds [Lewis *et al.*, 2013] or apply a threshold to develop a cloud and aerosol distinction algorithm [Morille *et al.*, 2007; L. Wang *et al.*, 2012]. Though not shown here, we used the convective condensation level (CCL) to estimate the base of clouds above the top of the boundary layer and then retrieve the CBLH under CCL. The results show that such a limiter is effective for decreasing the interference by clouds above the top of CBL. For the cases of boundary layer clouds, (e.g., fair weather cumulus topped on boundary layer), the cloud top is the boundary layer top. The CBLH from the lidar algorithm occurs either within or just above the cloud, depending on the specific conditions. In these cases, the presence of clouds will not interfere with the retrieval of CBLH.

### Acknowledgments

This work was supported by the National Nature Science Foundation of China (41375109), the Arid Meteorology Science Foundation of Institute of Arid Meteorology, China Meteorological Administration (CMA) (IAM201513), and the National Nature Science Foundation for Youths of China (41305027). We thank the Semi-Arid Climate and Environment Observatory of Lanzhou University (SACOL) for providing the observational data, and the data used for this paper are available for download after submitting an application at SACOL website ([http://climate.lzu.edu.cn/data/index\\_cn.asp](http://climate.lzu.edu.cn/data/index_cn.asp)). CMA provides the L-band sounding data at Yuzhong. We also thank Qian Huang, College of Atmospheric Sciences, Lanzhou University, for offering theoretical guidance.

### References

- André, J. C., G. De Moor, P. Lacarrere, G. Terry, and R. D. Vachat (1978), Modeling the 24-hour evolution of the mean and turbulent structures of the planetary boundary layer, *J. Atmos. Sci.*, *35*, 1861–1883, doi:10.1175/1520-0469(1978)035<1861:MTHEOT>2.0.CO;2.
- Baars, H., A. Ansmann, R. Engelmann, and D. Althausen (2008), Continuous monitoring of the boundary-layer top with lidar, *Atmos. Chem. Phys.*, *8*, 7281–7296, doi:10.5194/acp-8-7281-2008.
- Bian, J., H. Chen, H. Vömel, Y. Duan, Y. Xuan, and D. Lü (2011), Intercomparison of humidity and temperature sensors: GTS1, Vaisala RS80, and CFH, *Adv. Atmos. Sci.*, *28*, 139–146, doi:10.1007/s00376-010-9170-8.
- Boers, R., E. W. Eloranta, and R. L. Coulter (1984), Lidar observations of mixed layer dynamics: Tests of parameterized entrainment models of mixed layer growth rate, *J. Appl. Meteorol.*, *23*, 247–266, doi:10.1175/1520-0450(1984)023<0247:LOOMLD>2.0.CO;2.
- Bravo-Aranda, J. A., G. de-Arriba-Moreira, F. Navas-Guzmán, M. J. Granados-Muñoz, J. L. Guerrero-Rascado, D. Pozo-Vázquez, C. Arbizu-Barrena, F. J. Olmo, M. Mallet, and L. Alados-Arboledas (2016), PBL height estimation based on lidar depolarisation measurements (POLARIS), *Atmos. Chem. Phys. Discuss.*, doi:10.5194/acp-2016-718, in review.
- Brooks, I. M. (2003), Finding boundary layer top: Application of a wavelet covariance transform to lidar backscatter profiles, *J. Atmos. Oceanic Technol.*, *20*, 1092–1105, doi:10.1175/1520-0426(2003)020<1092:FBLTAO>2.0.CO;2.
- Campbell, J. R., D. L. Hlavka, E. J. Welton, C. J. Flynn, D. D. Turner, J. D. Spinhirne, V. S. Scott, and I. H. Wang (2002), Full-time, eye-safe cloud and aerosol Lidar observation at atmospheric radiation measurement program sites: Instruments and data processing, *J. Atmos. Oceanic Technol.*, *19*, 431–442, doi:10.1175/1520-0426(2002)019<0431:FTESCA>2.0.CO;2.
- Cohn, S. A., and W. M. Angevine (2000), Boundary layer height and entrainment zone thickness measured by lidars and wind-profiling radars, *J. Appl. Meteorol.*, *39*, 1233–1247, doi:10.1175/1520-0450(2000)039<1233:BLHAEZ>2.0.CO;2.
- Dang, R. J., H. Li, Z. G. Liu, and Y. Yang (2016), Statistical analysis of relationship between daytime lidar-derived planetary boundary layer height and relevant atmospheric variables in the semiarid region in northwest china, *Adv. Meteorol.*, *2016*, 13, doi:10.1155/2016/5375918.
- Davis, K. J., N. Gamage, C. R. Hagelberg, C. Kiemle, D. H. Lenschow, and P. P. Sullivan (2000), An objective method for deriving atmospheric structure from airborne lidar observations, *J. Atmos. Oceanic Technol.*, *17*, 1455–1468, doi:10.1175/1520-0426(2000)017<1455:AOMFDA>2.0.CO;2.
- Di, H. G., D. X. Hua, Y. F. Wang, and Q. Yan (2013), Investigation on the correction of the Mie scattering lidar's overlapping factor and echo signals over the total detection range, *Acta Phys. Sin.*, *62*, 94215–094215, doi:10.7498/aps.62.094215.
- Ding, J., X. Zhuge, Y. Wang, and A. Xiong (2015), Evaluation of Chinese aircraft meteorological data relay (AMDAR) weather reports, *J. Atmos. Oceanic Technol.*, *32*, 982–992, doi:10.1175/JTECH-D-14-00145.1.
- Driedonks, A. G. M., and H. Tennekes (1984), Entrainment effects in the well-mixed atmosphere boundary layer, *Boundary Layer Meteorol.*, *30*, 75–105, doi:10.1007/BF00121950.
- Du, C. L., S. Y. Liu, X. Yu, X. M. Li, C. Chen, Y. Peng, Y. Dong, Z. P. Dong, and F. Q. Wang (2013), Urban boundary layer height characteristics and relationship with particulate matter mass concentrations in Xi'an, Central China, *Aerosol Air Qual. Res.*, *13*, 1598–1607, doi:10.4209/aaqr.2012.10.0274.
- Elliott, W. P. (1958), The growth of the atmospheric internal boundary layer, *Eos Trans. AGU*, *39*, 1048–1054, doi:10.1029/TR039i006p01048.
- Emeis, S., K. Schäfer, and C. Münkel (2008), Surface-based remote sensing of the mixing-layer height—A review, *Meteorol. Z.*, *17*, 621–630, doi:10.1127/0941-2948/2008/0312.
- Eresmaa, N., A. Karppinen, S. M. Joffe, J. Räsänen, and H. Talvitie (2006), Mixing height determination by ceilometers, *Atmos. Chem. Phys.*, *6*, 1485–1493, doi:10.5194/acp-6-1485-2006.
- Farge, M. (1992), Wavelet transforms and their applications to turbulence, *Annu. Rev. Fluid Mech.*, *24*, 395–458, doi:10.1146/annurev.fl.24.010192.002143.
- Fernald, F. G., B. M. Herman, and J. A. Reagan (1972), Determination of aerosol height distributions by lidar, *J. Appl. Meteorol.*, *11*, 482–489, doi:10.1175/1520-0450(1972)011<0482:DOAHDB>2.0.CO;2.
- Flamant, C., J. Pelon, P. H. Flamant, and P. Durand (1997), Lidar determination of the entrainment zone thickness at the top of the unstable marine atmospheric boundary layer, *Boundary Layer Meteorol.*, *83*, 247–284, doi:10.1023/A:1000258318944.
- Granados-Muñoz, M. J., F. Navas-Guzmán, J. A. Bravo-Aranda, J. L. Guerrero-Rascado, H. Lyamani, J. Fernández-Gálvez, and L. Alados-Arboledas (2012), Automatic determination of the planetary boundary layer height using lidar: One-year analysis over southeastern Spain, *J. Geophys. Res.*, *117*, D18208, doi:10.1029/2012JD017524.
- Gryning, S.-E., and E. Batchvarova (1994), Parametrization of the depth of the entrainment zone above the daytime mixed layer, *Q. J. R. Meteorol. Soc.*, *120*, 47–58, doi:10.1002/qj.4971205150.
- Guo, J., et al. (2016), The climatology of planetary boundary layer height in china derived from radiosonde and reanalysis data, *Atmos. Chem. Phys.*, *16*, 13,309–13,319, doi:10.5194/acp-16-13309-2016.
- Hanna, S. R. (1987), An empirical formula for the height of the coastal internal boundary layer, *Boundary Layer Meteorol.*, *40*, 205–207, doi:10.1007/BF00140077.
- Hayden, K. L., K. J. Anlauf, R. M. Hoff, J. W. Strapp, J. W. Bottenheim, H. A. Wiebe, F. A. Froude, J. B. Martin, D. G. Steyn, and I. G. McKendry (1997), The vertical chemical and meteorological structure of the boundary layer in the lower Fraser Valley during Pacific'93, *Atmos. Environ.*, *31*, 2089–2105, doi:10.1016/S1352-2310(96)00300-7.
- Hennessy, B., and A. Lammert (2006), Determination of the atmospheric boundary layer height from radiosonde and lidar backscatter, *Boundary Layer Meteorol.*, *120*, 181–200, doi:10.1007/s10546-005-9035-3.
- Hooper, W. P., and E. W. Eloranta (1986), Lidar measurements of wind in the planetary boundary layer: The method, accuracy and results from joint measurements with radiosonde and kyttoon, *J. Clim. Appl. Meteorol.*, *25*, 990–1001, doi:10.1175/1520-0450(1986)025<0990:LMOWIT>2.0.CO;2.
- Hu, X.-M. (2015), Air pollution meteorology, in *Encyclopedia of Atmospheric Sciences*, 2nd ed., edited by G. R. North, J. Pyle, and F. Zhang, pp. 227–236, Academic Press, Oxford, U. K., doi: 10.1016/B978-0-12-382225-3.00499-0.
- Hu, X.-M., J. W. Nielsen-Gammon, and F. Zhang (2010a), Evaluation of three planetary boundary layer schemes in the WRF model, *J. Appl. Meteorol. Climatol.*, *49*, 1831–1844, doi:10.1175/2010JAMC2432.1.
- Hu, X.-M., J. M. Sigler, and J. D. Fuentes (2010b), Variability of ozone in the marine boundary layer of the equatorial pacific ocean, *J. Atmos. Chem.*, *66*, 117–136, doi:10.1007/s10874-011-9196-z.
- Huang, Z., J. Huang, J. Bi, G. Wang, W. Wang, Q. Fu, Z. Li, S.-C. Tsay, and J. Shi (2010), Dust aerosol vertical structure measurements using three MPL lidars during 2008 China-U.S. joint dust field experiment, *J. Geophys. Res.*, *115*, D00K15, doi:10.1029/2009JD013273.

- Huang, M., Z. Gao, S. Miao, F. Chen, M. A. Lemone, J. Li, F. Hu, and L. Wang (2016), Estimate of boundary-layer depth over Beijing, China, using Doppler lidar data during SURF-2015, *Boundary Layer Meteorol.*, *162*, 503, doi:10.1007/s10546-016-0205-2.
- Lammert, A., and J. Bösenberg (2006), Determination of the convective boundary-layer height with laser remote sensing, *Boundary Layer Meteorol.*, *119*, 159–170, doi:10.1007/s10546-005-9020-x.
- Lange, D., F. Rocadenbosch, J. Tiana-Alsina, and S. Frasier (2015), Atmospheric boundary layer height estimation using a Kalman filter and a frequency-modulated continuous-wave radar, *IEEE Trans. Geosci. Remote Sens.*, *53*, 3338–3349, doi:10.1109/TGRS.2014.2374233.
- Lewis, J. R., E. J. Welton, A. M. Molod, and J. Everette (2013), Improved boundary layer depth retrievals from MPLNET, *J. Geophys. Res. Atmos.*, *118*, 9870–9879, doi:10.1002/jgrd.50570.
- Lopes, F. J. S., G. A. Moreira, P. F. Rodrigues, J. L. Guerrero-Rascado, M. F. Andrade, and E. Landulfo (2014), Comparison between two algorithms based on different wavelets to obtain the planetary boundary layer height, *Proc. SPIE* 9246, Lidar Technologies, Techniques, and Measurements for Atmospheric Remote Sensing X, 92460H, doi: 10.1117/12.2067352.
- McGrath-Spangler, E. L., and A. S. Denning (2012), Estimates of North American summertime planetary boundary layer depths derived from space-borne lidar, *J. Geophys. Res.*, *117*, D15101, doi:10.1029/2012JD017615.
- Melfi, S. H., J. D. Spinhirne, S. H. Chou, and S. P. Palm (1985), Lidar observations of vertically organized convection in the planetary boundary layer over the ocean, *J. Appl. Meteorol. Climatol.*, *24*, 806–821, doi:10.1175/1520-0450(1985)024<0806:LOOVOC>2.0.CO;2.
- Menuet, L., C. Flamant, J. Pelon, and P. H. Flamant (1999), Urban boundary-layer height determination from lidar measurements over the Paris area, *Appl. Opt.*, *38*, 945–954, doi:10.1364/AO.38.000945.
- Morille, Y., M. Haeffelin, P. Drobinski, and J. Pelon (2007), STRAT: An automated algorithm to retrieve the vertical structure of the atmosphere from single-channel lidar data, *J. Atmos. Oceanic Technol.*, *24*, 761–775, doi:10.1175/JTECH2008.1.
- Nelson, E., R. Stull, and E. Eloranta (1989), A prognostic relationship for entrainment zone thickness, *J. Appl. Meteorol.*, *28*, 885–903, doi:10.1175/1520-0450(1989)028<0885:APRFEZ>2.0.CO;2.
- Nielsen-Gammon, J. W., C. L. Powell, M. J. Mahoney, W. M. Angevine, C. J. Senff, A. White, C. Berkowitz, C. Doran, and K. Knupp (2008), Multisensor estimation of mixing heights over a coastal city, *J. Appl. Meteorol. Climatol.*, *47*, 27–43, doi:10.1175/2007JAMC1503.1.
- Pal, S., M. Haeffelin, and E. Batchvarova (2013), Exploring a geophysical process-based attribution technique for the determination of the atmospheric boundary layer depth using aerosol lidar and near-surface meteorological measurements, *J. Geophys. Res. Atmos.*, *118*, 9277–9295, doi:10.1002/jgrd.50710.
- Rahn, D. A., and C. J. Mitchell (2016), Diurnal climatology of the boundary layer in Southern California using AMDAR temperature and wind profiles, *J. Appl. Meteorol. Climatol.*, *55*(5), 1123–1137, doi:10.1175/JAMC-D-15-0234.1.
- Sawyer, V., and Z. Li (2013), Detection, variations and intercomparison of the planetary boundary layer depth from radiosonde, lidar and infrared spectrometer, *Atmos. Environ.*, *79*, 518–528, doi:10.1016/j.atmosenv.2013.07.019.
- Seibert, P., F. Beyrich, S.-E. Gryning, S. Joffre, A. Rasmussen, and P. Tercier (2000), Review and intercomparison of operational methods for the determination of the mixing height, *Atmos. Environ.*, *34*, 1001–1027, doi:10.1016/S1352-2310(99)00349-0.
- Seidel, D. J., C. O. Ao, and K. Li (2010), Estimating climatological planetary boundary layer heights from radiosonde observations: Comparison of methods and uncertainty analysis, *J. Geophys. Res.*, *115*, D16113, doi:10.1029/2009JD013680.
- Senff, C., J. Bösenberg, G. Peters, and T. Schabert (1996), Remote sensing of turbulent ozone fluxes and the ozone budget in the convective boundary layer with DIAL and radar-RASS: A case study, *Contrib. Atmos. Phys.*, *69*, 161–176.
- Sicard, M., C. Pérez, F. Rocadenbosch, J. M. Baldasano, and D. García-Vizcaino (2006), Mixed-layer depth determination in the barcelona coastal area from regular lidar measurements: Methods, results and limitations, *Boundary Layer Meteorol.*, *119*, 135–157, doi:10.1007/s10546-005-9005-9.
- Spinhirne, J. D. (1993), Micro Pulse Lidar, *IEEE Trans. Geosci. Remote Sens.*, *31*, 48–54.
- Steyn, D. G., M. Baldi, and R. M. Hoff (1999), The detection of mixed layer depth and entrainment zone thickness from lidar backscatter profiles, *J. Atmos. Oceanic Technol.*, *16*, 953–959, doi:10.1175/1520-0426(1999)016<0953:DOMLD>2.0.CO;2.
- Stull, R. B. (1988), *An Introduction to Boundary Layer Meteorology*, pp. 13–16, Kluwer Acad., Dordrecht, Netherlands, doi: 10.1002/qj.49711548614.
- Tao, S. W., X. H. Chen, and J. D. Gong (2006), Error analyses for temperature of L-band radiosonde (in Chinese), *Meteorological*, *32*, 46–51.
- Tao, Z. M., Q. Z. Zhang, X. Fang, S. L. Wang, K. F. Cao, S. X. Hu, Y. F. Ji, and H. L. Hu (2009), Estimation of random errors for backscatter lidar observations, *Acta Photonica Sinica*, *38*, 3279–3282.
- Wang, Z., X. Cao, L. Zhang, J. Notholt, B. Zhou, R. Liu, and B. Zhang (2012), Lidar measurement of planetary boundary layer height and comparison with microwave profiling radiometer observation, *Atmos. Meas. Tech.*, *5*, 1965–1972, doi:10.5194/amtd-5-1233-2012.
- Wang, L., C. B. Xie, Z. Z. Wang, G. Y. Bo, D. Liu, and H. L. Wei (2012), Application of gradient method to detect height distribution of atmospheric boundary layer with lidar, *J. Atmos. Environ. Opt.*, *7*, 161–167, doi:10.3969/j.issn.1673-6141.2012.03.001.
- Welton, E. J., K. J. Voss, P. K. Quinn, P. J. Flatau, K. Markowicz, J. R. Campbell, J. D. Spinhirne, H. R. Gordon, and J. E. Johnson (2002), Measurement of aerosol vertical profiles and optical properties during INDOEX 1999 using micropulse lidars, *J. Geophys. Res.*, *107*(D19), 8019, doi:10.1029/2000JD000038.
- White, A. B., C. W. Fairall, and D. W. Thomson (1991), Radar observations of humidity variability in and above the marine atmospheric boundary layer, *J. Atmos. Oceanic Technol.*, *8*, 639–658, doi:10.1175/1520-0426(1991)008<0639:ROOHVI>2.0.CO;2.
- Yang, X. J., X. D. Xu, H. Y. Chen, S. Q. Ma, and W. M. Chen (2011), The analysis and correlation model of the surface layer information in L-band radiosonde high resolution profile (in Chinese), *Meteorol. Mon.*, *37*, 1504–1510.
- Zhang, Q., J. Zhang, J. Qiao, and S. Wang (2011), Relationship of atmospheric boundary layer depth with thermodynamic processes at the land surface in arid regions of China, *Earth Sci.*, *54*, 1586–1594, doi:10.1007/s11430-011-4207-0.
- Zhang, S. P., Z. P. Ren, J. W. Liu, Y. Q. Yang, and X. G. Wang (2008), Variations in the lower level of the PBL associated with the yellow sea fog-new observations by L-band radar, *J. Ocean Univ. Chin.*, *7*, 353–361, doi:10.1007/s11802-008-0353-1.
- Zhao, C. F., Y. Wang, Q. Wang, Z. Li, Z. Wang, and D. Liu (2014), A new cloud and aerosol layer detection method based on micropulse lidar measurements, *J. Geophys. Res. Atmos.*, *119*, 6788–6802, doi:10.1002/2014JD021760.
- Zhou, Z., and H. Adeli (2003), Time-frequency signal analysis of earthquake records using Mexican hat wavelets, *Comput. Aided Civ. Inf.*, *18*, 379–389, doi:10.1111/1467-8667.t01-1-00315.